

Acoustic Adiabatic Propagation Based on Topological Pumping in a Coupled Multicavity Chain Lattice

Ya-Xi Shen, Long-Sheng Zeng, Zhi-Guo Geng, De-Gang Zhao, Yu-Gui Peng, and Xue-Feng Zhu^{*}
School of Physics and Innovation Institute, Huazhong University of Science and Technology, Wuhan 430074, People's Republic of China



(Received 29 March 2020; revised 10 June 2020; accepted 15 June 2020; published 15 July 2020)

Stimulated adiabatic passage, as an efficient energy transfer in correlated systems, was intensively studied in condensed matter physics and quantum optics. Recently, a paradigm shift has been made to bring up quantum-classical analogs, giving rise to the acoustic version of stimulated Raman adiabatic passage and others. In this work, we focus on the adiabatic propagation of sound under topological protection, i.e., topological-pumping-based acoustic adiabatic propagation. We first study the topological pumping of sound in a two-state multicavity chain lattice, including the Su-Schrieffer-Heeger model, in which the acoustic energy is adiabatically transferred between the two topological end states under specific coupling interactions. Then, we consider the adiabatic propagation of sound via a dark mode in a three-state system. The three states correspond to two end states and one interface state in a heterostructured multicavity chain lattice, which is topologically protected. In a finite system, the three states strongly hybridize with the threefold energy degeneracy lifted. The hybridized states reside in the band gap of the systematic Hamiltonian spectrum in the topological pumping process, leading to a strong robustness against nonadiabatic perturbation, which allows for a faster and more efficient topological adiabatic propagation of acoustic waves.

DOI: 10.1103/PhysRevApplied.14.014043

I. INTRODUCTION

In the 1990s, researchers found a powerful technique, stimulated Raman adiabatic passage (STIRAP) [1–9], that enabled complete and selective population transfer in the three-level systems by means of two overlapping interactions with counterintuitive action sequences. For STIRAP, a particularly interesting feature is that population transfer between the initial state and final state does not suffer any losses from the intermediate radiative state. The physics behind this is that the transfer is completed via a dark mode that does not involve intermediate states in the dynamic process. The intriguing properties of STIRAP, such as robustness against small variations of the interaction and intermediate radiative damping, have stimulated researchers to extend this scheme from atomic and molecular physics [10–13], quantum information [14–16], and solid-state physics [17–20] to classical physics [21–26]. In acoustics, an analog of STIRAP was proposed recently, where the cavities and pseudo-time-varying coupling actions act as discrete states and the laser pulses in a quantum system, respectively [26]. The technique of STIRAP can be extended into multilevel systems. For the acoustic counterpart of STIRAP, it thus requires multicavity chain systems with time-varying coupling interactions.

Previous studies have shown that the acoustic adiabatic energy transmission via a dark state can be implemented only when the number of cavities is odd [26–30]. To realize acoustic STIRAP in an odd-number cavity chain, it is crucial that the evolution of the system needs to satisfy the adiabatic limit. A sufficient condition for the adiabatic evolution is $\Delta\epsilon = |\epsilon_n - \epsilon_m| \gg |\dot{\psi}_n(t)\psi_m(t)|$ [3,6,26–30], where ϵ_n , ϵ_m , $\psi_n(t)$, and $\psi_m(t)$ are adjacent eigenenergies and corresponding eigenstates of the systematic Hamiltonian, and the overdot indicates differentiation with respect to time. In general, the eigenenergy difference, $\Delta\epsilon$, between the adiabatic transfer state, $\psi_n(t)$, and its adjacent eigenstate, $\psi_m(t)$, is very small. Therefore, to satisfy the adiabatic limit, the time evolution of the adiabatic transfer state should be very slow due to a trivial $\Delta\epsilon$. Thus, if we want to relax the adiabatic limit condition, it is intuitive to increase the eigenenergy difference, $\Delta\epsilon$, to form a nontrivial band gap in the Hamiltonian spectrum. For efficient and robust acoustic adiabatic propagation, it is more interesting to make the adiabatic transfer state in a band gap topologically nontrivial. By combining topological insulators [31–45] with the acoustic adiabatic passage, we can realize robust excitation transfer among topologically protected end states, which is also termed as topological pumping. As aforementioned, in topological pumping, we purposefully make the topological transfer state away from the continuum bands over the whole adiabatic process,

* xfzhu@hust.edu.cn

which otherwise will result in the degradation of transfer efficiency.

Here, we first analyze acoustic adiabatic passage in an odd-number cavity chain with randomly distributed time-varying coupling coefficients. In this case, the eigenenergy difference between the adiabatic transfer state and its adjacent eigenstates is very small. Thus, an extremely slow evolution is required to complete the adiabatic propagation of sound from the first cavity of the system to the last one. In the next step, we focus on the topological propagation of end states in the one-dimensional (1D) Su-Schrieffer-Heeger (SSH) cavity chain lattice, where the staggered time-varying coupling coefficients $\kappa_1(t)$ and $\kappa_2(t)$ are applied. For 1D SSH cavity chain lattices, the eigenenergies of the system are divided into two parts with a band gap of width $2|\kappa_1(t) - \kappa_2(t)|$. The topologically protected end states reside in the band gap, except for the critical point at $\kappa_1(t) = \kappa_2(t)$. Finally, we study the effect of topological STIRAP, where two end states and one interface state under topological protection are constructed by splicing two types of SSH cavity chains. In the heterostructured SSH cavity chain, the three topologically protected states hybridize with each other and the corresponding eigenenergies are lifted. It should be pointed out that the hybridized states remain in the band gap of the Hamiltonian spectrum during the overall adiabatic interaction. By combining STIRAP with topological pumping, the adiabatic transfer of sound energy can be both efficient and robust.

II. ACOUSTIC ADIABATIC PROPAGATION IN AN ODD-NUMBER MULTICAVITY CHAIN SYSTEM

For an acoustic cavity chain with odd-numbered cavities ($N = 2n + 1$), as shown in Fig. 1(a), the adiabatic

evolution of sound, as a result of slowly varying couplings, can be well described by a Schrödinger-type equation [46]

$$i\frac{d}{dt}\psi(t) = H(t)\psi(t), \quad (1)$$

where $\psi(t)$ and $H(t)$ denote the transient state function and time-dependent Hamiltonian of the system, respectively. The transient state function $\psi(t)$ can be mapped into the parameter coordinate space of $\{\varphi_1, \varphi_2, \dots, \varphi_N\}$ and be expressed as $\psi(t) = \sum_{i=1}^N a_i(t)\varphi_i$, where $a_i(t)$ is the sound amplitude in each cavity. According to the tight-binding approximation, the systematic Hamiltonian, $H(t)$, can be written into a matrix of

$$H(t) = \begin{pmatrix} 0 & c_{1,2}(t) & 0 & \cdots & 0 & 0 \\ c_{1,2}(t) & 0 & c_{2,3}(t) & \cdots & 0 & 0 \\ 0 & c_{2,3}(t) & 0 & \cdots & 0 & 0 \\ \vdots & \vdots & \vdots & \ddots & \vdots & \vdots \\ 0 & 0 & 0 & \cdots & 0 & c_{N-1,N}(t) \\ 0 & 0 & 0 & \cdots & c_{N-1,N}(t) & 0 \end{pmatrix}, \quad (2)$$

where $c_{i,j}(t)$ is the coupling coefficient between two adjacent cavities, and all cavities are identical and lossless. By solving Eq. (2), there exists an adiabatic transfer state, $\phi_0(t)$, corresponding to the zero eigenenergy, i.e., $\varepsilon = 0$. This adiabatic transfer state connects the first cavity of the system with the last one, for which the normalized form is [26]

$$\phi_0(t) = \alpha(t)(1, 0, \chi_1, 0, \chi_2\chi_1, 0, \dots, \prod_{i=1}^n \chi_i)^T, \quad (3)$$

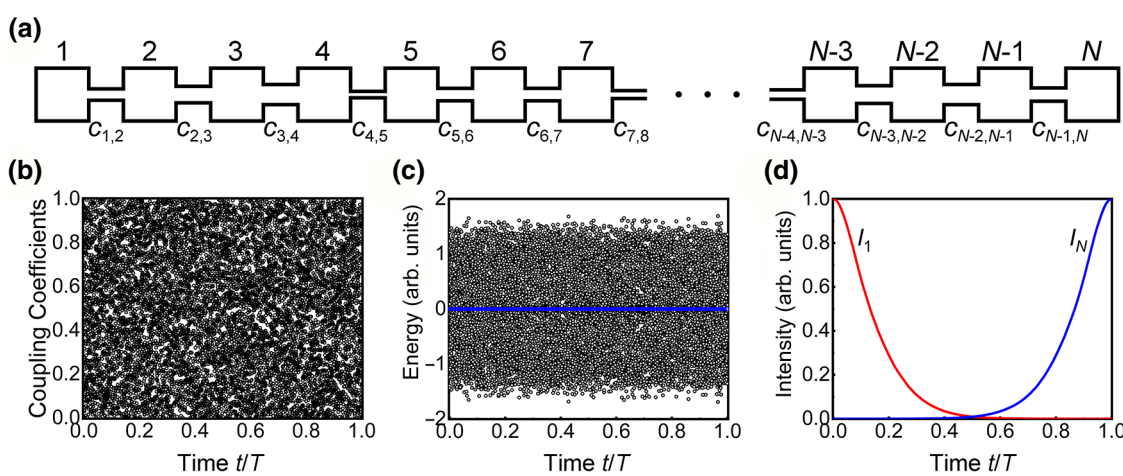


FIG. 1. (a) Schematic of the odd-number cavity chain with coupling interactions between adjacent cavities. (b) Time evolution of coupling coefficients randomly taking values in the range of $c_{ij}(t) \in [0, 1]$. (c) Time evolution of the Hamiltonian spectrum of the multicavity chain system. (d) Normalized sound intensities in cavities 1 (red solid) and N (blue solid), when the coupling interaction satisfies the adiabatic limit. In numerical calculations, the number of cavities is $N = 21$.

where $\alpha(t)$ is the normalization factor and $\chi_k(t) = -c_{2k-1,2k}(t)/c_{2k,2k+1}(t)$, in which $k = 1, 2, \dots, n$. From Eq. (3), we can clearly see that the ratio between the sound amplitudes in the odd-numbered cavity, $2k + 1$, and the first cavity, 1, is

$$\frac{a_{2k+1}(t)}{a_1(t)} = \chi_1(t)\chi_2(t) \cdots \chi_k(t). \quad (4)$$

By setting $k = n$, we eventually obtain the ratio between the sound amplitudes in the last cavity, N , and the first cavity, 1

$$\frac{a_N(t)}{a_1(t)} = \chi_1(t)\chi_2(t) \cdots \chi_n(t). \quad (5)$$

Without loss of generality, we assume that all time-varying coupling coefficients are changed in the range of $c_{ij}(t) \in [0, 1]$ and are randomly combined, as shown in Fig. 1(a). From Eqs. (3)–(5), we find that, when the coupling interaction is set at $\chi_1(t)\chi_2(t) \cdots \chi_n(t) \xrightarrow{t \rightarrow 0} 0$ and $\chi_1(t)\chi_2(t) \cdots \chi_n(t) \xrightarrow{t \rightarrow T} +\infty$, the sound energy will be transferred from the initially excited cavity, 1, to the last cavity, N , along the adiabatic transfer state, $\phi_0(t)$. Figures 1(b) and 1(c) show the time evolution of the coupling coefficients $c_{ij}(t)$ over the interaction and the corresponding evolution of the Hamiltonian spectrum. In numerical calculations, the cavity number is $N = 21$. In Fig. 1(c), we can see that the Hamiltonian spectrum is irregular, except for the zero-value eigenenergy (blue circles). The eigenenergy difference, $\Delta\epsilon$, between the zero-eigenenergy (or adiabatic) transfer state and its adjacent eigenstate is very small during the interaction. Thus, in light of the adiabatic limit, to realize the adiabatic transmission of sound energy from the initial cavity to the last one, we need to guarantee

that the evolution of the systematic Hamiltonian, $H(t)$, is extremely slow. In other words, the interaction time, T , of the acoustic adiabatic passage should be very long. Here, we show the calculation results of the acoustic adiabatic passage under the adiabatic limit in Fig. 1(d), where the time evolution of the normalized sound intensities in cavities 1 and N are calculated by solving Schrödinger-type Eqs. (1) and (2). Figure 1(d) shows that the sound energy can be completely transferred from cavity 1 to cavity N after the adiabatic interaction.

III. TOPOLOGICAL-PUMPING-BASED ADIABATIC PROPAGATION IN THE ACOUSTIC TWO-STATE SYSTEMS

A. Model and theory

In this section, we consider a special situation in Eq. (5), i.e., $\chi_k(t) \equiv \chi(t)$, $k = 1, 2, \dots, n$. In this case, the acoustic multicavity chain becomes a truncated SSH model, where each unit cell consists of two sites: A and B . As shown in Fig. 2(a), the staggered coupling coefficients $\kappa_1(t) = c_{2k-1,2k}(t)$ and $\kappa_2(t) = c_{2k,2k+1}(t)$ denote the intra-cell and intercell coupling coefficients, respectively. At the limit of $N \rightarrow +\infty$, the physical properties of the SSH cavity chain lattice should depend on the bulk instead of the boundary condition. Imposing the Born-von Karman boundary condition on the SSH cavity chain lattice, the bulk Hamiltonian $H(t)$ can be expressed as

$$H(t) = \sum_{m=1}^n (\kappa_1 \hat{B}_m^\dagger \hat{A}_m + \kappa_2 \hat{A}_{m+1}^\dagger \hat{B}_m + H.c.), \quad (6)$$

where $\hat{A}_m^\dagger(\hat{A}_m)$ and $\hat{B}_m^\dagger(\hat{B}_m)$ are the creation (annihilation) operators at sites A and B , respectively, on unit cell m .

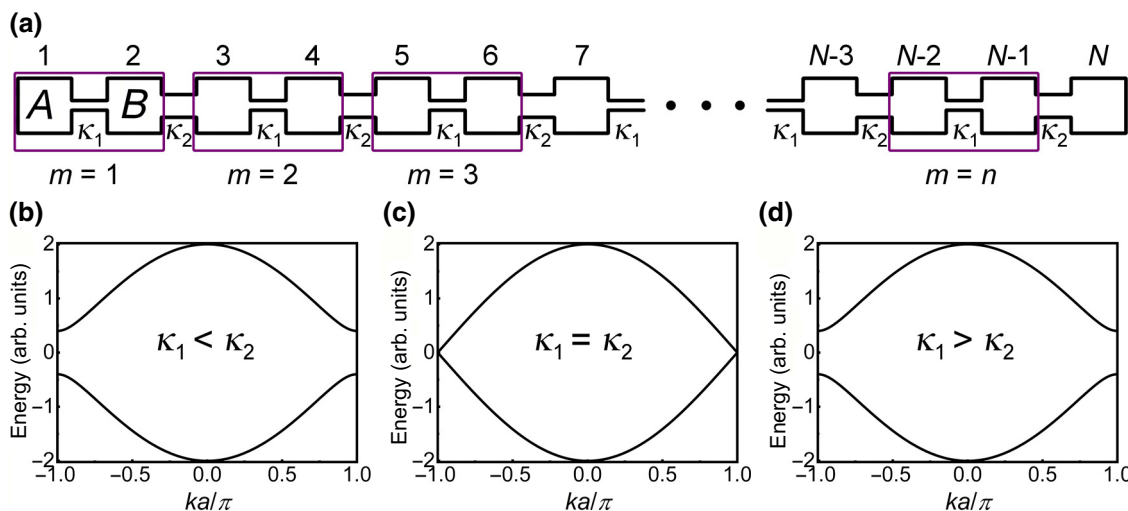


FIG. 2. (a) Schematic of the finite SSH cavity chain with staggered coupling coefficients κ_1 and κ_2 . Eigenenergy spectra of the SSH cavity chain lattice for three different coupling coefficients of $\kappa_1 < \kappa_2$ (b), $\kappa_1 = \kappa_2$ (c), and $\kappa_1 > \kappa_2$ (d).

Performing the Fourier transformation, we obtain

$$\hat{A}_k = \frac{1}{\sqrt{n}} \sum_m e^{-ikma} \hat{A}_m, \quad (7a)$$

$$\hat{B}_k = \frac{1}{\sqrt{n}} \sum_m e^{-ikma} \hat{B}_m, \quad (7b)$$

where a is the lattice constant. Thus, we can derive an alternative form of the systematic Hamiltonian in k space

$$H = \sum_k \psi_k^\dagger H_k \psi_k, \quad (8)$$

where $\psi_k = (\hat{A}_k^\dagger, \hat{B}_k^\dagger)^T$ and $\hat{A}_k^\dagger, \hat{B}_k^\dagger$ are the creation operators on sites A and B , respectively, at wave number k . For each wave number k , the bulk momentum-space Hamiltonian H_k can be expressed as

$$H_k = \begin{pmatrix} 0 & \kappa_1 + \kappa_2 e^{-ika} \\ \kappa_1 + \kappa_2 e^{ika} & 0 \end{pmatrix}, \quad (9)$$

with $k \in [-\pi/a, \pi/a]$. By solving Eq. (9), we obtain the eigenenergies of the bulk momentum-space Hamiltonian H_k

$$\varepsilon_-(k) = -\sqrt{\kappa_1^2 + \kappa_2^2 + 2\kappa_1\kappa_2 \cos(ka)}, \quad (10a)$$

$$\varepsilon_+(k) = \sqrt{\kappa_1^2 + \kappa_2^2 + 2\kappa_1\kappa_2 \cos(ka)}. \quad (10b)$$

The corresponding eigenstates are

$$\varphi_-(k) = \frac{1}{\sqrt{2}} \begin{pmatrix} 1 \\ -\kappa_1 - \kappa_2 e^{ika} \end{pmatrix}, \quad (11a)$$

$$\varphi_+(k) = \frac{1}{\sqrt{2}} \begin{pmatrix} 1 \\ \kappa_1 + \kappa_2 e^{ika} \end{pmatrix}. \quad (11b)$$

Analyzing Eqs. (10a) and (10b), we can clearly see that the eigenenergy spectrum of the system is divided into two bands, i.e., the negative eigenenergy band $\varepsilon_-(k)$ and the positive eigenenergy band $\varepsilon_+(k)$. Figures 2(b)–2(d) show the bulk dispersion relations of the SSH cavity chain lattices with three different coupling coefficients, $\kappa_1 < \kappa_2$ in Fig. 2(b), $\kappa_1 = \kappa_2$ in Fig. 2(c), and $\kappa_1 > \kappa_2$ in Fig. 2(d).

For the case of $\kappa_1 = \kappa_2$ in Fig. 2(c), we observe that the band gap is closed at the boundaries of the first Brillouin zone ($k = \pm\pi/a$). The SSH chain is more like a “conductor.” In Figs. 2(b) and 2(d), there exists a band gap with width $2|\kappa_1 - \kappa_2|$, separating the positive eigenenergy band

$\varepsilon_+(k)$ from the negative eigenenergy band $\varepsilon_-(k)$, where the staggered coupling coefficients $\kappa_1 \neq \kappa_2$. It is noted that the band gaps at $\kappa_1 > \kappa_2$ and $\kappa_1 < \kappa_2$ are topologically trivial and nontrivial, respectively, which can be proved by calculating the Zak phase of the eigenstate $\varphi_-(k)$ [33,34]

$$\gamma = \int_{-\pi/a}^{\pi/a} [\varphi_-^\dagger(k) i \partial_k \varphi_-(k)] dk. \quad (12)$$

Substituting Eq. (11a) into Eq. (12), we obtain the Zak phases $\gamma = \pi$ and $\gamma = 0$ for the cases of $\kappa_1 < \kappa_2$ and $\kappa_1 > \kappa_2$, respectively. In the topologically nontrivial phase ($\kappa_1 < \kappa_2$), the SSH cavity chain sustains robust end states for an open boundary truncated at the intercell coupling channel [33,34]. However, for a finite SSH chain with odd-numbered cavities $N = 2n + 1$, the right-side end is cut at the intracell coupling channel and the whole chain is asymmetric. Therefore, there will be only one topologically protected end state in the band gap. From Eq. (3), the end state can be expressed as

$$\phi_0(t) = \alpha(1, 0, \chi, 0, \chi^2, 0, \dots, \chi^n)^T, \quad (13)$$

where $\chi = -\kappa_1/\kappa_2$. Since $\chi^n \xrightarrow{n \rightarrow +\infty} 0$, the end state is thus localized on the left-side cavities from Eq. (13). Here, we define the end state as $\phi_0 = \phi_L$. At the limit $\chi \rightarrow 0$, the end state ϕ_L is completely localized at the first cavity of the system. According to the normalization condition $\langle \phi_L | \phi_L \rangle = 1$, we further express the topologically protected end state as

$$\phi_L = \alpha_L(1, 0, \chi, 0, \chi^2, 0, \chi^3, 0, \dots)^T, \quad \kappa_1 < \kappa_2, \quad (14)$$

where the normalization factor is $\alpha_L = \sqrt{(1 - \chi^2)/(1 - \chi^{2n+2})}$. In another case, for coupling coefficients $\kappa_1 > \kappa_2$, the SSH cavity chain is flipped, with the end state localized on the right-side cavities. We define the end state as $\phi_0 = \phi_R$, which can be expressed as

$$\phi_R = \alpha_R(\dots, 0, \eta^3, 0, \eta^2, 0, \eta, 0, 1)^T, \quad \kappa_1 > \kappa_2, \quad (15)$$

where $\eta = -\kappa_2/\kappa_1$ and the normalization factor is $\alpha_R = \sqrt{(1 - \eta^2)/(1 - \eta^{2n+2})}$. Thus, the adiabatic transfer state of the system can take the evolution from $\phi_0 \xrightarrow{\kappa_1 < \kappa_2} \phi_L$ to $\phi_0 \xrightarrow{\kappa_1 > \kappa_2} \phi_R$. In the limits of $\phi_L \xrightarrow{\kappa_1/\kappa_2 \rightarrow 0} \varphi_1$ and $\phi_R \xrightarrow{\kappa_2/\kappa_1 \rightarrow 0} \varphi_N$, we eventually realize the topological-pumping-based adiabatic propagation of sound in an acoustic SSH cavity chain by $\phi_0(t) = \varphi_1 \rightarrow \varphi_N$ with $\kappa_1(t)/\kappa_2(t) = 0 \rightarrow +\infty$.

To quantitatively describe the topologically protected adiabatic propagation of sound in a SSH cavity chain lattice, we consider the time-varying coupling coefficients

$\kappa_1(t)$ and $\kappa_2(t)$ as follows:

$$\kappa_1(t) = \kappa_0[1 - \cos(\pi t/T)], \quad (16a)$$

$$\kappa_2(t) = \kappa_0[1 + \cos(\pi t/T)], \quad (16b)$$

where $\kappa_0 = 0.5$ and $\kappa_1(t), \kappa_2(t) \in [0, 1]$. Figure 3(a) shows the changing curves of the time-varying coupling coefficients $\kappa_1(t)$ and $\kappa_2(t)$ during the interaction time. The time evolution of the instantaneous energy spectrum of the systematic Hamiltonian $H(t)$ is shown in Fig. 3(b), where the cavity number is $N = 21$. From Fig. 3(b), we can clearly observe that the topologically protected adiabatic transfer states (the blue line) reside in the band gap of the Hamiltonian spectrum. Comparing Fig. 3(b) with Fig. 1(c), we conclude that the topological adiabatic propagation in the SSH cavity chain is much more robust and efficient due to the existence of the nontrivial band gap between the adiabatic transfer state and its adjacent bulk states. However, at the thermodynamic limit of $N \rightarrow +\infty$, the band gap is closed at $t = T/2$, where $\kappa_1 = \kappa_2$. An example is given in Fig. 3(c) with the cavity number $N = 1001$. As a result, the local adiabatic limit condition cannot always be fulfilled during the interaction, since the energy difference between the adiabatic transfer state and its adjacent eigenstates $\Delta\varepsilon = 0$ at the transition point $\kappa_1 = \kappa_2$. Figure 3(d) shows the normalized sound intensities in cavities 1 (red line) and N (blue line) during interaction time T , by numerically solving Eqs. (1) and (2). After one adiabatic cycle, the sound energy is completely transferred

from cavity 1 of the system to cavity N . Figures 3(e)–3(i) display the normalized sound-intensity distributions of the adiabatic transfer state at five different times of $t = 0$, $t = T/3$, $t = T/2$, $t = 2T/3$, and $t = T$, respectively. The results show that the end state is localized on the left-side cavities of the SSH cavity chain for $\kappa_1 < \kappa_2$ and is completely captured in the first cavity at the limit $\kappa_1/\kappa_2 \rightarrow 0$, as shown in Figs. 3(e) and 3(f). When the coupling coefficients are tuned to be $\kappa_1 > \kappa_2$, the end state becomes localized on the right-side cavities of the SSH cavity chain and is completely captured in the last cavity at the limit $\kappa_2/\kappa_1 \rightarrow 0$, as shown in Figs. 3(h) and 3(i). It is noted that, in Fig. 3(g), the sound energy is fully delocalized into the bulk at $\kappa_1 = \kappa_2$.

B. Design of coupling coefficients between neighboring cavities

The design of coupling coefficients is pivotal for the experimental realization of topological adiabatic propagation of sound in the multicavity chain system. For a rectangular cavity, eigenmode frequencies can be expressed as $f_m = mc_0/2h$, where m is the order of eigenmodes in the height direction, and $c_0 = 343$ m/s is the speed of sound in air. Figure 4(a) shows the sound-intensity profile of the second-order eigenmode in a single cavity, which is an even mode with maxima located at the center and two ends of the cavity. For a two-cavity system, as shown in

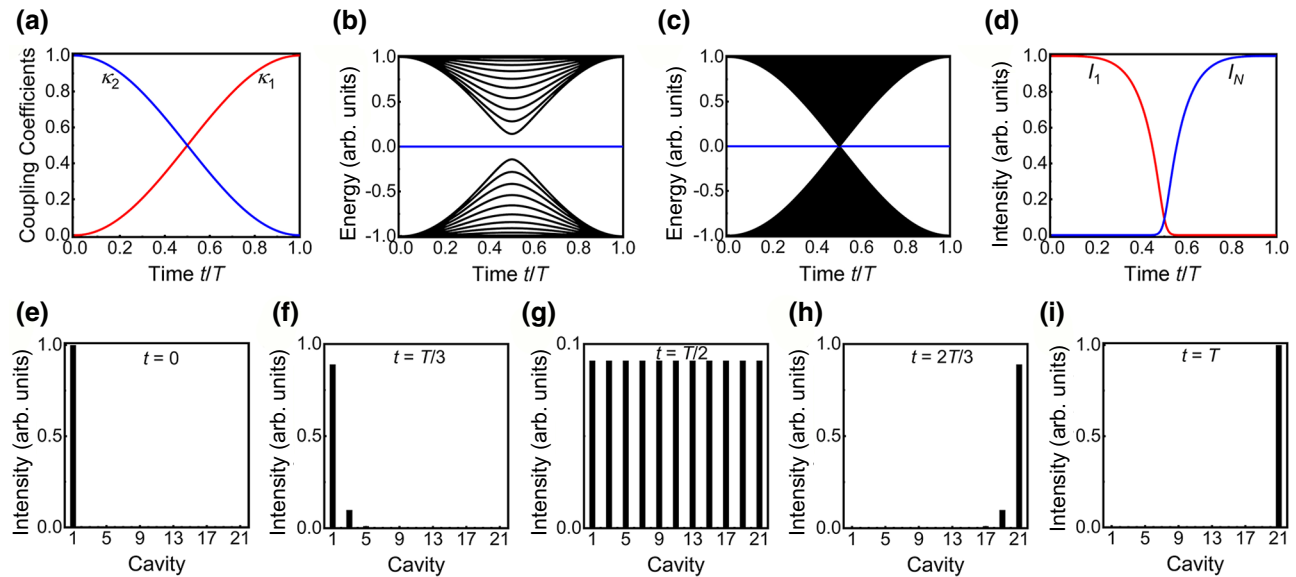


FIG. 3. (a) Changes of the coupling coefficients $\kappa_1(t), \kappa_2(t)$ versus time t . (b), (c) Eigenenergy spectra of the systematic Hamiltonian $H(t)$, where the number of cavities $N = 21$ (b) and $N = 1001$ (c). (d) Normalized intensities in the cavities 1 (the red line) and N (the blue line). Normalized intensity distributions of the adiabatic transfer state at five different times of $t = 0$ (e), $t = T/3$ (f), $t = T/2$ (g), $t = 2T/3$ (h), and $t = T$ (i).

Fig. 4(b), the systematic Hamiltonian H can be written as

$$H = \begin{pmatrix} \delta_0 & c \\ c & \delta_0 \end{pmatrix}, \quad (17)$$

where c denotes the coupling coefficient between two identical cavities, and δ_0 is the eigenmode frequency of a single cavity. By solving Eq. (17), we obtain the eigenvalues

$$\varepsilon_1 = \delta_0 - c, \quad (18a)$$

$$\varepsilon_2 = \delta_0 + c. \quad (18b)$$

Then, the coupling coefficient can be expressed as

$$c = (\varepsilon_2 - \varepsilon_1)/2. \quad (19)$$

From Eq. (19), we can obtain the coupling coefficient c by calculating the difference in eigenenergies of the two-cavity system. For high-order modes in the two-cavity system, the coupling coefficient between cavities is related to the size of the coupling channel and is proportional to the product of pressure amplitudes at the two ends of the coupling channel [47,48].

Figures 4(c) and 4(d) show the numerical calculation of coupling coefficients in different cases, where the width and height of the cavities are set to be $d = 30$ mm and $h = 100$ mm, respectively. In Fig. 4(c), the coupling channel is fixed at $y = 0$ mm and the length is $l = 20$ mm,

while the width w is changed from 0.1 to 20 mm. The result shows that the coupling coefficient enlarges as the width w increases. Fixing the size of the coupling channel ($l = 20$ mm and $w = 10$ mm), the coupling coefficient can also be tuned by moving the coupling channel along the y direction in the range of $y \in [-25, 25]$ mm, as shown in Fig. 4(d). Because of the even symmetry of the second-order eigenmode, the coupling coefficient should be an even function with respect to y . Our result shows that the coupling curve can be accurately fitted by a cosine-type function, $c(y) = c_0[1 + \cos(2\pi y/D)]$, where $c_0 = 76.3 \text{ s}^{-1}$ and $D = 50$ mm. Figure 4(e) shows the sound-intensity profiles in the two-cavity systems that correspond to three different structures of $(w = 5 \text{ mm}, y = 0 \text{ mm})$, $(w = 10 \text{ mm}, y = 0 \text{ mm})$, and $(w = 10 \text{ mm}, y = 10 \text{ mm})$. To realize a time-varying coupling coefficient, we further assume that the coupling channel moves linearly and slowly in time, by following $y = v_0 t + y_0$ and $y \in [-25, 25]$ mm, where v_0 and y_0 are the preset moving speed and initial position, respectively. We eventually obtain the time-varying coupling coefficient $c(t) = c_0[1 + \cos(2\pi(v_0 t + y_0)/D)]$. In practice, the coupled multicavity system with sliding connective channels can be implemented as shown in Fig. 5, where the coupling channel is schematically located at $y = -D/2$, $y = 0$, and $y = D/2$ in Figs. 5(a)–5(c), respectively. Here, D is half of the cavity height. Therefore, we can obtain a time-varying coupling coefficient by linearly and slowly moving the coupling channel in the range of $[-D/2, D/2]$.

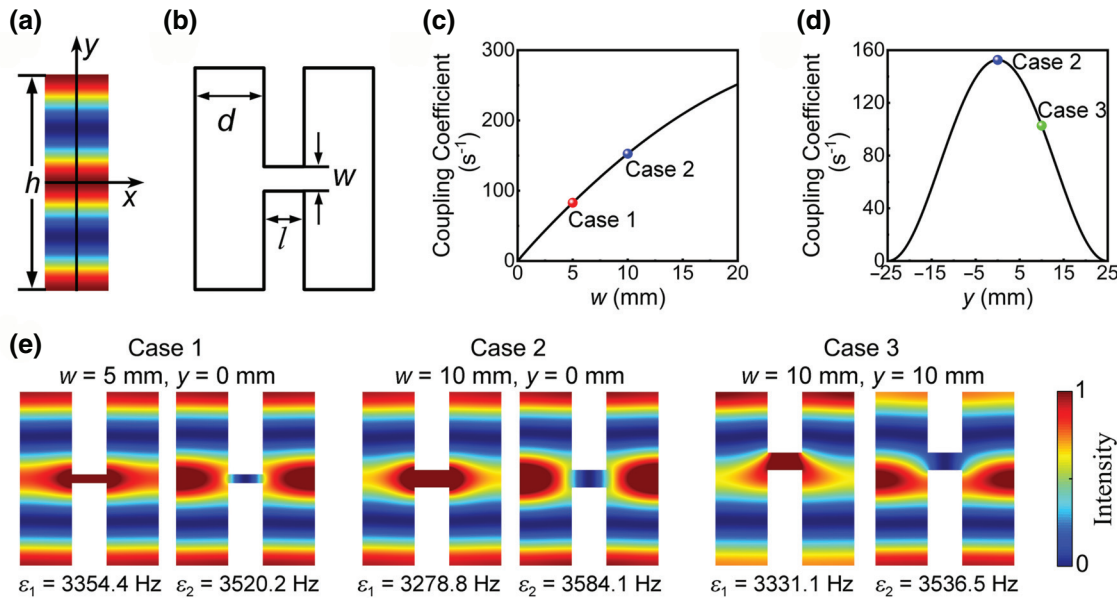


FIG. 4. (a) Sound-intensity profile of the second-order eigenmode in a single cavity. (b) Schematic of the two-cavity system. (c) Coupling coefficient versus the width (w) of the air channel, where the air channel is fixed at $y = 0$ mm, with other structural parameters of $h = 100$ mm, $d = 30$ mm, and $l = 20$ mm. (d) Coupling coefficient versus the coupling position y , where the channel width is set at $w = 10$ mm. (e) Sound-intensity profiles in three different two-cavity systems, which correspond to sets of $(w = 5 \text{ mm}, y = 0 \text{ mm})$, $(w = 10 \text{ mm}, y = 0 \text{ mm})$, and $(w = 10 \text{ mm}, y = 10 \text{ mm})$, with the eigenfrequencies appended below.

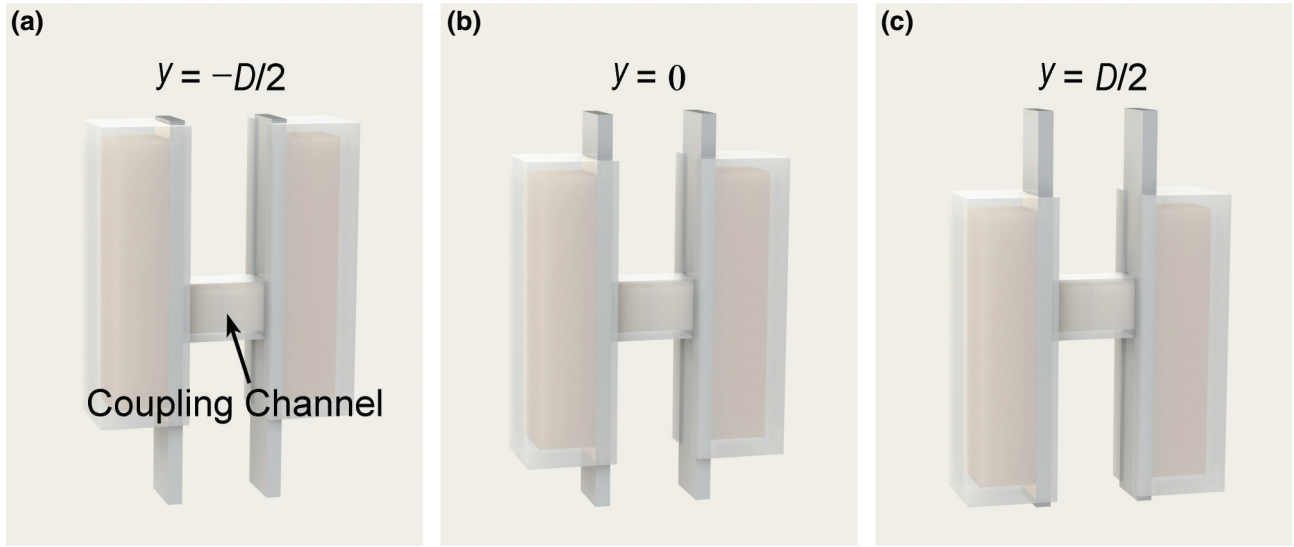


FIG. 5. Schematic of the coupling interaction in a two-cavity acoustic system. correspond to cases that the coupling channel locates at $y = -D/2$ (a), $y = 0$ (b), and $y = D/2$ (c).

C. Topological-pumping-based acoustic adiabatic propagation

The topological adiabatic propagation in a designed acoustic system is demonstrated via the pressure acoustic module of the COMSOL Multiphysics™ 5.3a program. In full-wave simulations, the structural parameters of the cavities are chosen to be those in case 1 of Fig. 4(e). By moving the coupling channels, we obtain the cosine-shaped time-varying coupling coefficients $\kappa_1(t)$ and $\kappa_2(t)$

$$\kappa_1(t) = \kappa_0[1 - \cos(\pi t/T)], \quad (20a)$$

$$\kappa_2(t) = \kappa_0[1 + \cos(\pi t/T)], \quad (20b)$$

where $\kappa_0 = 41.5 \text{ s}^{-1}$.

Figure 6(a) presents the designed time-varying coupling coefficients $\kappa_1(t)$ and $\kappa_2(t)$ versus time t . The corresponding eigenenergy spectrum of the systematic Hamiltonian $H(t)$ is shown in Fig. 6(b), where the cavity number is $N = 21$. The result reveals that the topological adiabatic states reside in the band gap of the Hamiltonian spectrum. Figure 6(c) shows the sound-intensity distributions of the adiabatic transfer state in the designed structure at five different times of $t = 0$, $t = T/3$, $t = T/2$, $t = 2T/3$, and $t = T$. We find that the adiabatic transfer state is localized on the left-side (right-side) cavities of the system for $\kappa_1 < \kappa_2$ ($\kappa_1 > \kappa_2$). Specifically, at $t = 0$ ($\kappa_1/\kappa_2 = 0$), the adiabatic transfer state is completely captured in the first cavity. At $t = T/2$ ($\kappa_1 = \kappa_2$), the sound energy spreads into the full SSH cavity chain. At $t = T$ ($\kappa_2/\kappa_1 = 0$), the adiabatic transfer state is completely captured in the last cavity. The numerical simulation results agree well with

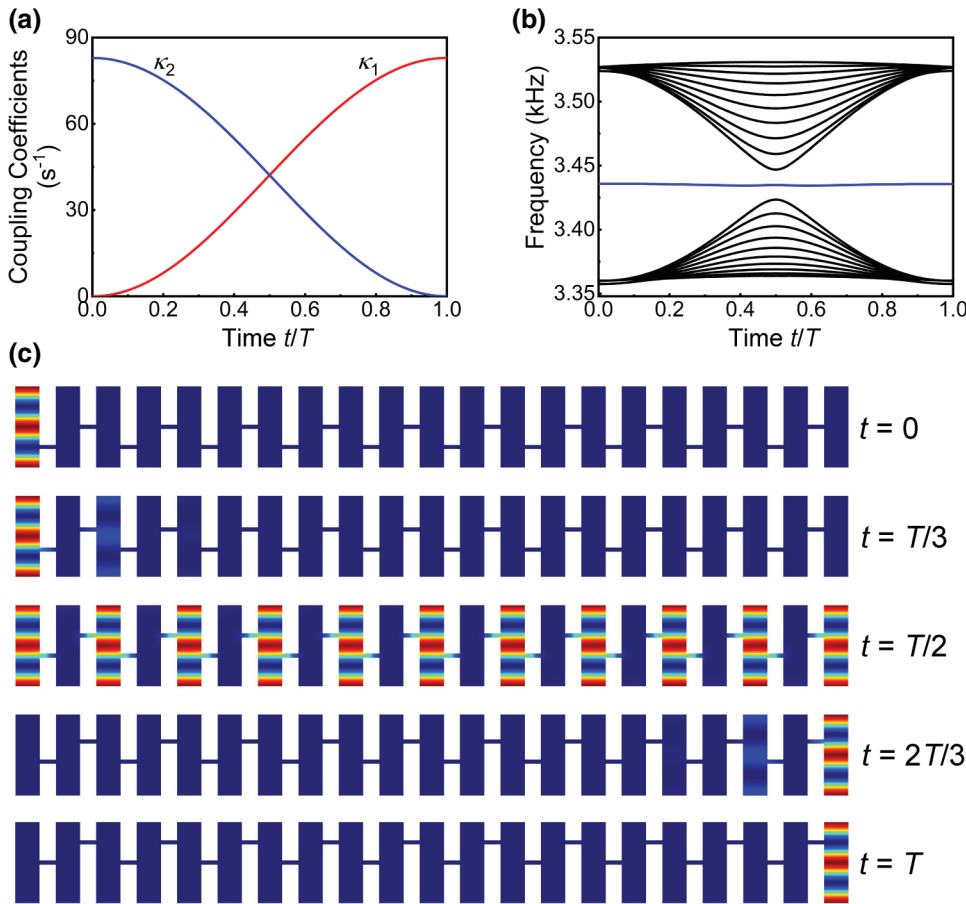
the above theoretical analyses. In addition, by mapping the time dimension (t axis) into an orthogonal space dimension (for example, z axis), the topologically protected adiabatic transfer of sound energy can also be realized in the coupled waveguide systems, in which the time-varying coupling coefficients are replaced by position-dependent coupling coefficients that are adiabatically changed along the direction of sound propagation [26].

IV. TOPOLOGICAL-PUMPING-BASED ADIABATIC PROPAGATION IN ACOUSTIC THREE-STATE SYSTEMS

A. The construction of topological end states and interface state

In this section, we utilize two different SSH cavity chains to construct two end states and one interface state, which are under topological protection [35,45]. Figures 7(a) and 7(b) show two types of the interfaces that correspond to weak and strong coupling combinations, respectively. Here, the number of cavities is $N = 2n + 1$. The time-varying coupling coefficients are $\tau_1(t)$ and $\tau'_1(t)$, with constant τ_2 and $\tau_1(t)$, $\tau'_1(t) < \tau_2$. The interface can also be considered as a domain wall between two SSH cavity chains with different topological invariants. As schematically shown in Figs. 7(a) and 7(b), the domain walls support a single-cavity mode and a trimer-cavity mode, respectively. For the case of the single-cavity domain wall in Fig. 7(a), we define the topologically protected states as $\phi_L^1(t)$, $\phi_C^1(t)$, and $\phi_R^1(t)$, which can be written as

$$\phi_L^1(t) = \alpha_L^1(t)(1, 0, \chi(t), 0, \chi^2(t), 0, \chi^3(t), 0, \dots)^T, \quad (21a)$$



$$\phi_C^I(t) = \alpha_C^I(t)(\dots, \chi^2(t), 0, \chi(t), 0, 1, 0, \eta(t), 0, \eta^2(t), \dots)^T, \quad (21b)$$

$$\phi_R^I(t) = \alpha_R^I(t)(\dots, 0, \eta^3(t), 0, \eta^2(t), 0, \eta(t), 0, 1)^T, \quad (21c)$$

where the variables are $\chi(t) = -\tau_1(t)/\tau_2$ and $\eta(t) = -\tau'_1(t)/\tau_2$, and the normalization factors are $\alpha_L^I(t) = \sqrt{(1-\chi^2)/(1-\chi^{n+1})}$, $\alpha_C^I(t) = 1/\sqrt{(1-\chi^{n+1})/(1-\chi^2) + (1-\eta^{n+1})/(1-\eta^2) - 1}$, and $\alpha_R^I(t) = \sqrt{(1-\eta^2)/(1-\eta^{n+1})}$, with n being an odd number. Since $\langle \phi_i^I(t) | \phi_j^I(t) \rangle = \delta_{ij}$, $i, j \in \{L, C, R\}$, the three

topologically protected states, $\phi_L^I(t)$, $\phi_C^I(t)$, and $\phi_R^I(t)$, are normalized and orthogonal. At the limit of $N \rightarrow +\infty$, the topologically protected states $\phi_L^I(t)$, $\phi_C^I(t)$, and $\phi_R^I(t)$ are exactly the eigenstates of the systematic Hamiltonian $H(t)$ with degenerate eigenenergies. In a finite-cavity system, the topologically protected states hybridize with each other and the eigenenergies are lifted. However, the hybridized states remain in the band gap of the instantaneous Hamiltonian spectrum during the adiabatic interaction. At the limit of $\tau_1(t)/\tau_2 \rightarrow 0$, $\tau'_1(t)/\tau_2 \rightarrow 0$ (i.e., $\chi(t), \eta(t) \rightarrow 0$), the topologically protected states $\phi_L^I(t)$, $\phi_C^I(t)$, and $\phi_R^I(t)$ are completely localized in cavities 1, $n+1$, and N , respectively. For the case of the trimer-cavity domain wall in Fig. 7(b), the topologically protected states can be

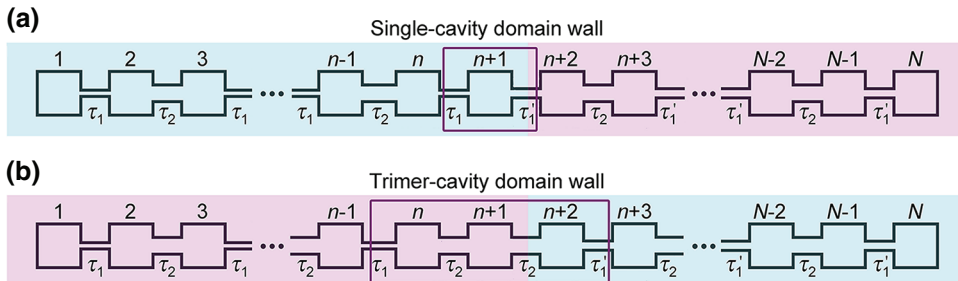


FIG. 7. (a) Schematic of the heterostructured SSH cavity chain with a single-cavity domain wall. (b) Schematic of the heterostructured SSH cavity chain with a trimer-cavity domain wall.

expressed as

$$\phi_L^{\text{II}}(t) = \alpha_L^{\text{II}}(t)(1, 0, \chi(t), 0, \chi^2(t), 0, \chi^3(t), 0, \dots)^T, \quad (22\text{a})$$

$$\phi_C^{\text{II}}(t) = \alpha_C^{\text{II}}(t)(\dots, \chi^2(t), 0, \chi(t), 0, 1, 0, 1, 0, \eta(t), 0, \eta^2(t), \dots)^T, \quad (22\text{b})$$

$$\phi_R^{\text{II}}(t) = \alpha_R^{\text{II}}(t)(\dots, 0, \eta^3(t), 0, \eta^2(t), 0, \eta(t), 0, 1)^T, \quad (22\text{c})$$

where the variables are $\chi(t) = -\tau_1(t)/\tau_2$ and $\eta(t) = -\tau'_1(t)/\tau_2$, and the normalization factors are $\alpha_L^{\text{II}}(t) = \sqrt{(1 - \chi^2)/(1 - \chi^n)}$, $\alpha_C^{\text{II}}(t) = 1/\sqrt{(1 - \chi^n)/(1 - \chi^2) + (1 - \eta^n)/(1 - \eta^2)}$, and $\alpha_R^{\text{II}}(t) = \sqrt{(1 - \eta^2)/(1 - \eta^n)}$, with n being an even number. Here, the topologically protected states $\phi_L^{\text{II}}(t)$, $\phi_C^{\text{II}}(t)$, and $\phi_R^{\text{II}}(t)$ are also normalized and orthogonal, and thus, $\langle \phi_i^{\text{II}}(t) | \phi_j^{\text{II}}(t) \rangle = \delta_{ij}$, $i, j \in \{L, C, R\}$. In a finite acoustic system, these states hybridize and the hybridized eigenenergies remain in the band gap. Different from the case in Fig. 7(a), the topologically protected interface state $\phi_C^{\text{II}}(t)$ is localized in the cavities n and $n+2$ at the limit of $\tau_1(t)/\tau_2 \rightarrow 0$ and $\tau'_1(t)/\tau_2 \rightarrow 0$.

B. Acoustic analog of the topological STIRAP

For the three-state acoustic systems, we can employ the technique of STIRAP to implement the adiabatic propagation of sound energy. We first consider the case in Fig. 7(a). By using the localized states at the cavity domain walls to construct a subspace $\{\phi_L^{\text{I}}(t), \phi_C^{\text{I}}(t), \phi_R^{\text{I}}(t)\}$, we approximately express the transient state in the subspace under the adiabatic elimination of the other eigenstates as follows:

$$\psi(t) \cong a_L \phi_L^{\text{I}} + a_C \phi_C^{\text{I}} + a_R \phi_R^{\text{I}}. \quad (23)$$

In the subspace, we obtain the coupling relations

$$\begin{aligned} \langle \phi_L^{\text{I}}(t) | H(t) | \phi_L^{\text{I}}(t) \rangle &= \langle \phi_C^{\text{I}}(t) | H(t) | \phi_C^{\text{I}}(t) \rangle \\ &= \langle \phi_R^{\text{I}}(t) | H(t) | \phi_R^{\text{I}}(t) \rangle = 0, \end{aligned} \quad (24\text{a})$$

$$\langle \phi_L^{\text{I}}(t) | H(t) | \phi_R^{\text{I}}(t) \rangle = \langle \phi_R^{\text{I}}(t) | H(t) | \phi_L^{\text{I}}(t) \rangle = 0, \quad (24\text{b})$$

$$\langle \phi_L^{\text{I}}(t) | H(t) | \phi_C^{\text{I}}(t) \rangle = \langle \phi_C^{\text{I}}(t) | H(t) | \phi_L^{\text{I}}(t) \rangle = C_L(t), \quad (24\text{c})$$

$$\langle \phi_C^{\text{I}}(t) | H(t) | \phi_R^{\text{I}}(t) \rangle = \langle \phi_R^{\text{I}}(t) | H(t) | \phi_C^{\text{I}}(t) \rangle = C_R(t), \quad (24\text{d})$$

where the effective coupling coefficients between the adjacent topological states are $C_L(t) = \alpha_L^{\text{I}} \alpha_C^{\text{I}} \{[(n+1)/2]\tau_1$

$\chi^{(n-1)/2} + [(n-1)/2]\tau_2 \chi^{(n-1)/2}\}$ and $C_R(t) = \alpha_R^{\text{I}} \alpha_C^{\text{I}} \{[(n+1)/2]\tau'_1 \eta^{(n-1)/2} + [(n-1)/2]\tau_2 \eta^{(n-1)/2}\}$. The effective systematic Hamiltonian $H(t)$ of the topological three-state system can be written as

$$H(t) = \begin{pmatrix} 0 & C_L(t) & 0 \\ C_L(t) & 0 & C_R(t) \\ 0 & C_R(t) & 0 \end{pmatrix}. \quad (25)$$

Solving Eq. (25), the eigenvalues are

$$\varepsilon_{-}(t) = -\sqrt{C_L^2(t) + C_R^2(t)}, \quad (26\text{a})$$

$$\varepsilon_0(t) = 0, \quad (26\text{b})$$

$$\varepsilon_{+}(t) = \sqrt{C_L^2(t) + C_R^2(t)}. \quad (26\text{c})$$

The corresponding eigenstates are

$$\phi_{-}(t) = \frac{\sin \theta(t)}{\sqrt{2}} \phi_L^{\text{I}} - \frac{1}{\sqrt{2}} \phi_C^{\text{I}} + \frac{\cos \theta(t)}{\sqrt{2}} \phi_R^{\text{I}}, \quad (27\text{a})$$

$$\phi_0(t) = \cos \theta(t) \phi_L^{\text{I}} - \sin \theta(t) \phi_R^{\text{I}}, \quad (27\text{b})$$

$$\phi_{+}(t) = \frac{\sin \theta(t)}{\sqrt{2}} \phi_L^{\text{I}} + \frac{1}{\sqrt{2}} \phi_C^{\text{I}} + \frac{\cos \theta(t)}{\sqrt{2}} \phi_R^{\text{I}}, \quad (27\text{c})$$

where $\theta(t) = \arctan[C_L(t)/C_R(t)]$. In the effective topological three-state system, the adiabatic transfer state $\phi_0(t)$ can be considered to be a dark state, since the topological interface state ϕ_C^{I} is not excited during the whole propagation process. When the cavity chain system is well tailored to satisfy $C_L(t)/C_R(t) \xrightarrow{t \rightarrow t_0} 0$ and $C_L(t)/C_R(t) \xrightarrow{t \rightarrow T} +\infty$, the parameter $\theta(t)$ varies from zero to $\pi/2$, as the time t changes from t_0 to T . Under the adiabatic limit, from Eq. (27b), we find that the adiabatic transfer state $\phi_0(t)$ transits from the topological end state ϕ_L^{I} to an intermediate superposition of the topological states ϕ_L^{I} and ϕ_R^{I} and, in the end, is completely transferred to the topological end state ϕ_R^{I} . In addition, since the end states are $\phi_L^{\text{I}} \xrightarrow{\tau_1(t)/\tau_2 \rightarrow 0} \varphi_1$ and $\phi_R^{\text{I}} \xrightarrow{\tau'_1(t)/\tau_2 \rightarrow 0} \varphi_N$, we eventually realize the topological adiabatic propagation in the system of $\phi_0(t) = \varphi_1 \rightarrow \varphi_N$ via a dark state. To quantitatively investigate the topological adiabatic propagation in the heterostructured SSH

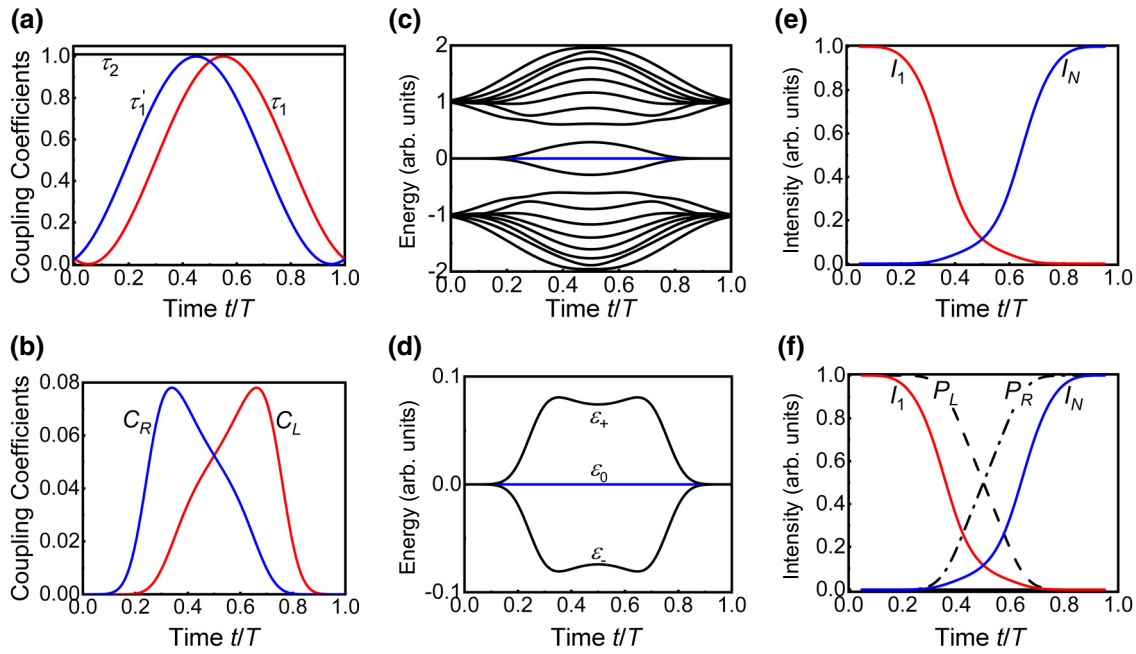


FIG. 8. (a) Coupling coefficients $\tau_1(t)$, $\tau'_1(t)$, and τ_2 versus time t , where $\tau_1(t), \tau'_1(t) \in [0, 1]$, and $\tau_2 = 1.01 > \tau_1(t), \tau'_1(t)$. (b) Effective coupling coefficients $C_L(t)$ and $C_R(t)$, which are obtained via the approximate three-state description. (c) Instantaneous eigenenergy spectrum of the systematic Hamiltonian $H(t)$. In the calculation, the cavity number is $N = 19$. (d) Hybridized eigenenergies based on the approximate three-state description. Normalized sound intensities in cavities 1 (red line) and N (blue line), which are calculated by solving the Schrödinger-type equation (e) and by the approximate three-state description (f).

cavity chain systems, we assume that the time-varying coupling coefficients $\tau_1(t)$ and $\tau'_1(t)$ are

$$\tau_1(t) = \tau_0 \left[1 - \cos \frac{2\pi(t - \Delta t)}{T} \right], \quad (28a)$$

$$\tau'_1(t) = \tau_0 \left[1 - \cos \frac{2\pi(t + \Delta t)}{T} \right], \quad (28b)$$

where $\Delta t = 0.05T$, $\tau_0 = 0.5$, $\tau_1(t), \tau'_1(t) \in [0, 1]$, and $\tau_2 = 1.01 > \tau_1(t), \tau'_1(t)$. Figure 8(a) shows the time-varying coupling coefficients $\tau_1(t)$, $\tau'_1(t)$, and τ_2 versus time t , where a counterintuitive interaction is applied with $\tau'_1(t)$ preceding to $\tau_1(t)$. The corresponding effective coupling coefficients $C_L(t)$ and $C_R(t)$ are plotted in Fig. 8(b) and also manifest a counterintuitive interaction with $C_R(t)$ preceding to $C_L(t)$. Figure 8(c) shows the instantaneous energy spectrum of the systematic Hamiltonian $H(t)$, where the cavity number is $N = 19$ in the numerical calculation. In Fig. 8(c), we find that a band gap exists with three hybridized topological states residing inside, which is expected to provide strong robustness against the nonadiabatic effect and allow for a faster and more efficient transfer process. Figure 8(d) shows the hybridized eigenenergies based on the approximate three-state description. Figures 8(e) and 8(f) describe the evolution of normalized sound intensities in cavities 1 (red line) and N (blue line)

line), which are calculated by solving the Schrödinger-type equation and by the approximate three-state description, respectively. The results show that the sound energy in the system is completely transferred from cavity 1 to cavity N after the adiabatic interaction. The black dashed line and the black dotted and dashed line in Fig. 8(f) denote the probability evolution, $P_{L,R}(t)$, of the topological end states $\phi_L^1(t)$ and $\phi_R^1(t)$. Comparing Fig. 8(e) with Fig. 8(f), we conclude that it is feasible to implement the topological adiabatic propagation of sound via the technique of STIRAP. For the case of the trimer-cavity domain wall in Fig. 7(b), the aforementioned process is also valid, with the effective coupling coefficients being $C_L(t) = \alpha_L^{II}\alpha_C^{II}\{(n/2)\tau_1\chi^{(n/2)-1} + [(n-2)/2]\tau_2\chi^{n/2}\}$ and $C_R(t) = \alpha_R^{II}\alpha_C^{II}\{(n/2)\tau'_1\eta^{(n/2)-1} + [(n-2)/2]\tau_2\eta^{n/2}\}$.

C. Topological adiabatic propagation of sound in the heterostructured SSH cavity chain

In this section, we present the topological adiabatic propagation in the designed three-state acoustic system. In the simulation, the width of the coupling channels is $w = 10$ mm and the other parameters are the same as those of the two-state topological pumping in Fig. 6. In this case, we obtain the coupling coefficients

$$\tau_1(t) = \tau_0 \left[1 - \cos \frac{2\pi(t - \Delta t)}{T} \right], \quad (29a)$$

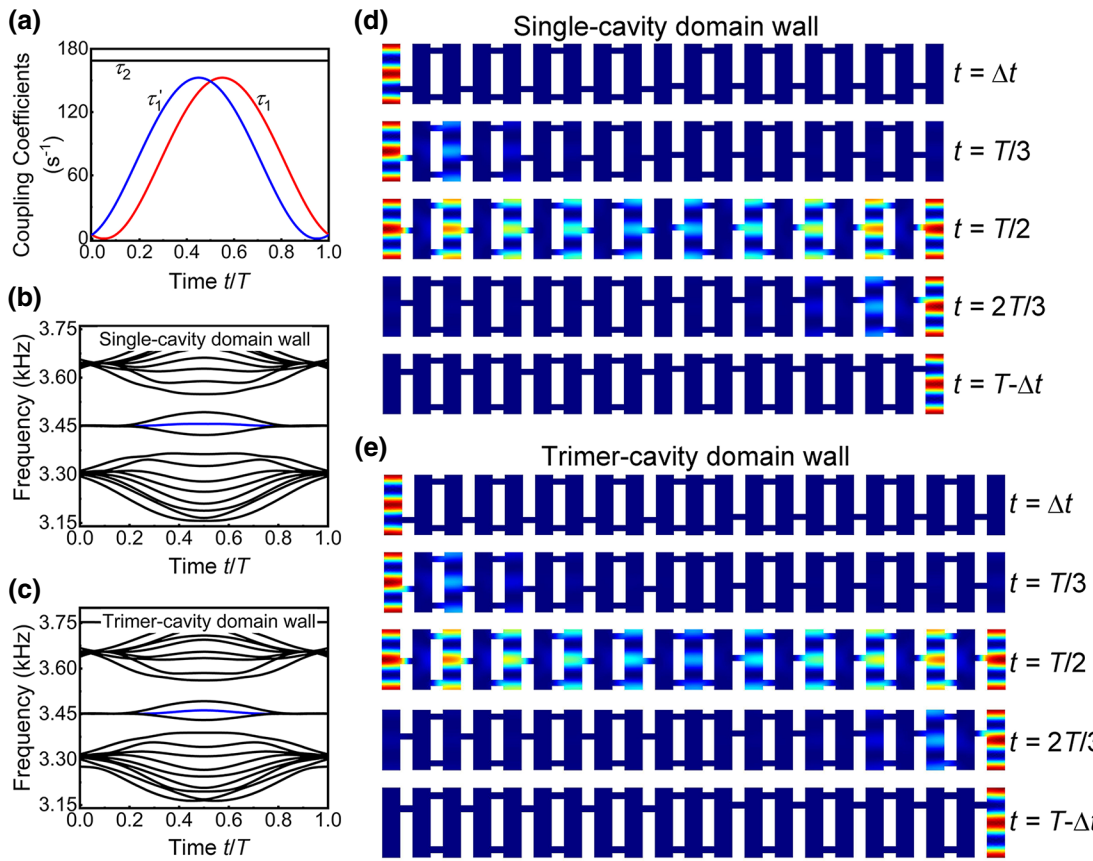


FIG. 9. (a) Time-varying coupling coefficients $\tau_1(t)$, $\tau'_1(t)$, and τ_2 versus time t in the designed structure. Eigenfrequency spectra of the designed structures with single-cavity (b) and trimer-cavity (c) domain walls at the interface. Sound-intensity distributions of the topologically protected adiabatic transfer state $\phi_0(t)$ at five different instants of time $t = \Delta t$, $t = T/3$, $t = T/2$, $t = 2T/3$, and $t = T - \Delta t$, for structures with single-cavity (d) and trimer-cavity (e) domain walls.

$$\tau'_1(t) = \tau_0 \left[1 - \cos \frac{2\pi(t + \Delta t)}{T} \right], \quad (29b)$$

$$\tau_2 = 168.8 \text{ s}^{-1}, \quad (29c)$$

where $\Delta t = 0.05T$ and $\tau_0 = 76.3 \text{ s}^{-1}$.

Figure 9(a) shows the changing curves of the designed coupling coefficients $\tau_1(t)$, $\tau'_1(t)$, and τ_2 . Figures 9(b) and 9(c) display the simulated eigenfrequency spectra of the designed structures with single-cavity and trimer-cavity domain walls, respectively. In agreement with theory, the hybridized topological states reside in the band gap. In Figs. 9(d) and 9(e), we plot sound-intensity distributions of the topological adiabatic transfer state $\phi_0(t)$ at five different times of $t = \Delta t$, $t = T/3$, $t = T/2$, $t = 2T/3$, and $t = T - \Delta t$, for the designed structures with single-cavity and trimer-cavity domain walls, respectively. At the beginning of time $t = \Delta t$, the coupling interaction $\tau_1(t)/\tau_2 = 0$ and the topological adiabatic transfer state is completely localized in the first cavity. At the end of time $t = T - \Delta t$, the coupling interaction $\tau'_1(t)/\tau_2 = 0$ and the

topological adiabatic transfer state is completely localized in the last cavity. During the adiabatic interaction process, the sound energy is transferred from the first cavity to the last one. Comparing Fig. 9 with Fig. 8, we find that the numerical simulation results agree well with the theoretical analyses.

V. CONCLUSIONS

In summary, we comprehensively investigate the topological adiabatic propagation of sound in the two-state and three-state time-varying SSH cavity chain lattices. Without requiring an extremely slow evolution to complete adiabatic transfer in gapless acoustic systems, we find that the topological pumping of end states in the SSH cavity chains is protected by a nontrivial band gap with a width of $2|\kappa_1(t) - \kappa_2(t)|$, which provides a strong robustness against the nonadiabatic effect and allows for a faster and more efficient transfer. We design structures for the experimental implementation of topological-pumping-based acoustic adiabatic propagation and verify the effectiveness in transferring sound energy between two robust

end states in full-wave simulations. The physics and design rules can be further extended to the heterostructured SSH cavity chain, where two end states and one interface state under topological protection are employed to construct a topological three-state system. We find that, in this architecture, topological pumping can be judiciously fused with the acoustic STIRAP technique. As a useful result, efficient and robust adiabatic transfer of sound energy is realized in the band gap of the Hamiltonian spectrum between two topological end states via a dark state.

ACKNOWLEDGMENTS

This work is supported by the National Natural Science Foundation of China (Grants No. 11674119, No. 11690030, and No. 11690032). X.-F.Z. would like to acknowledge financial support from the Bird Nest Plan of HUST.

-
- [1] U. Gaubatz, P. Rudecki, S. Schiemann, and K. Bergmann, Population transfer between molecular vibrational levels by stimulated Raman scattering with partially overlapping laser fields: A new concept and experimental results, *J. Chem. Phys.* **92**, 5363 (1990).
 - [2] B. W. Shore, Examples of counter-intuitive physics, *Contemp. Phys.* **36**, 15 (1995).
 - [3] T. A. Laine and S. Stenholm, Adiabatic processes in three-level systems, *Phys. Rev. A* **53**, 2501 (1996).
 - [4] K. Bergmann, H. Theuer, and B. W. Shore, Coherent population transfer among quantum states of atoms and molecules, *Rev. Mod. Phys.* **70**, 1003 (1998).
 - [5] N. V. Vitanov, T. Halfmann, B. W. Shore, and K. Bergmann, Laser-induced population transfer by adiabatic passage techniques, *Annu. Rev. Phys. Chem.* **52**, 763 (2001).
 - [6] B. W. Shore, Coherent manipulations of atoms using laser light, *Acta Phys. Slovaca* **58**, 243 (2008).
 - [7] K. Bergmann, N. V. Vitanov, and B. W. Shore, Perspective: Stimulated Raman adiabatic passage: The status after 25 years, *J. Chem. Phys.* **142**, 170901 (2015).
 - [8] N. V. Vitanov, A. A. Rangelov, B. W. Shore, and K. Bergmann, Stimulated Raman adiabatic passage in physics, chemistry, and beyond, *Rev. Mod. Phys.* **89**, 015006 (2017).
 - [9] K. Bergmann, Roadmap on STIRAP applications, *J. Phys. B: At. Mol. Opt. Phys.* **52**, 202001 (2019).
 - [10] L. S. Goldner, C. Gerz, R. J. C. Spreeuw, S. L. Rolston, C. I. Westbrook, W. D. Phillips, P. Marte, and P. Zoller, Momentum Transfer in Laser-Cooled Cesium by Adiabatic Passage in a Light Field, *Phys. Rev. Lett.* **72**, 997 (1994).
 - [11] Y. X. Du, Z. T. Liang, W. Huang, H. Yan, and S. L. Zhu, Experimental observation of double coherent stimulated Raman adiabatic passages in three-level Λ systems in a cold atomic ensemble, *Phys. Rev. A* **90**, 023821 (2014).
 - [12] T. Takekoshi, L. Reichsöllner, A. Schindewolf, J. M. Hutton, C. R. L. Sueur, O. Dulieu, F. Ferlaino, R. Grimm, and H. C. Nägerl, Ultracold Dense Samples of Dipolar RbCs Molecules in the Rovibrational and Hyperfine Ground State, *Phys. Rev. Lett.* **113**, 205301 (2014).
 - [13] M. Y. Guo, B. Zhu, B. Lu, X. Ye, F. D. Wang, R. Vexiau, N. Bouloufa-Maafa, G. Quéméner, O. Dulieu, and D. J. Wang, Creation of an Ultracold gas of Ground-State Dipolar $^{23}\text{Na}_{87}\text{Rb}$ Molecules, *Phys. Rev. Lett.* **116**, 205303 (2016).
 - [14] X. Lacour, N. Sangouard, S. Guérin, and H. R. Jauslin, Arbitrary state controlled-unitary gate by adiabatic passage, *Phys. Rev. A* **73**, 042321 (2006).
 - [15] D. Møller, L. B. Madsen, and K. Mølmer, Geometric phases in open tripod systems, *Phys. Rev. A* **77**, 022306 (2008).
 - [16] B. Rousseaux, S. Guérin, and N. V. Vitanov, Arbitrary qudit gates by adiabatic passage, *Phys. Rev. A* **87**, 032328 (2013).
 - [17] H. Goto and K. Ichimura, Population transfer via stimulated Raman adiabatic passage in a solid, *Phys. Rev. A* **74**, 053410 (2006).
 - [18] J. Klein, F. Beil, and T. Halfmann, Robust Population Transfer by Stimulated Raman Adiabatic Passage in a $\text{Pr}^{3+}:\text{Y}_2\text{SiO}_5$ Crystal, *Phys. Rev. Lett.* **99**, 113003 (2007).
 - [19] D. A. Golter and H. Wang, Optically Driven Rabi Oscillations and Adiabatic Passage of Single Electron Spins in Diamond, *Phys. Rev. Lett.* **112**, 116403 (2014).
 - [20] H. K. Xu, C. Song, W. Y. Liu, G. M. Xue, F. F. Su, H. Deng, Y. Tian, D. N. Zheng, S. Y. Han, Y. P. Zhong, H. Wang, Y. X. Liu, and S. P. Zhao, Coherent population transfer between uncoupled or weakly coupled states in ladder-type superconducting qutrits, *Nat. Commun.* **7**, 11018 (2016).
 - [21] S. Longhi, Adiabatic passage of light in coupled optical waveguides, *Phys. Rev. E* **73**, 026607 (2006).
 - [22] S. Longhi, G. Della Valle, M. Ornigotti, and P. Laporta, Coherent tunneling by adiabatic passage in an optical waveguide system, *Phys. Rev. B* **76**, 201101(R) (2007).
 - [23] G. Della Valle, M. Ornigotti, T. Toney Fernandez, P. Laporta, S. Longhi, A. Coppa, and V. Foglietti, Adiabatic light transfer via dressed states in optical waveguide arrays, *Appl. Phys. Lett.* **92**, 011106 (2008).
 - [24] F. Dreisow, A. Szameit, M. Heinrich, R. Keil, S. Nolte, A. Tünnermann, and S. Longhi, Adiabatic transfer of light via a continuum in optical waveguides, *Opt. Lett.* **34**, 2405 (2009).
 - [25] R. Menchon-Enrich, A. Benseny, V. Ahufinger, A. D. Greentree, T. Busch, and J. Mompart, Spatial adiabatic passage: A review of recent progress, *Rep. Prog. Phys.* **79**, 074401 (2016).
 - [26] Y. X. Shen, Y. G. Peng, D. G. Zhao, X. C. Chen, J. Zhu, and X. F. Zhu, One-way Localized Adiabatic Passage in an Acoustic System, *Phys. Rev. Lett.* **122**, 094501 (2019).
 - [27] B. W. Shore, K. Bergmann, J. Oreg, and S. Rosenwaks, Multilevel adiabatic population transfer, *Phys. Rev. A* **44**, 7442 (1991).
 - [28] F. T. Hioe and C. E. Carroll, Coherent population trapping in N -level quantum systems, *Phys. Rev. A* **37**, 3000 (1988).
 - [29] N. V. Vitanov, Adiabatic population transfer by delayed laser pulses in multistate systems, *Phys. Rev. A* **58**, 2295 (1998).
 - [30] C. Ciret, V. Coda, A. A. Rangelov, D. N. Neshev, and G. Montemazzani, Broadband adiabatic light transfer in optically induced waveguide arrays, *Phys. Rev. A* **87**, 013806 (2013).
 - [31] W. P. Su, J. R. Schrieffer, and A. J. Heeger, Solitons in Polyacetylene, *Phys. Rev. Lett.* **42**, 1698 (1979).

- [32] D. J. Thouless, Quantization of particle transport, *Phys. Rev. B* **27**, 6083 (1983).
- [33] S. Q. Shen, *Topological Insulators: Dirac Equation in Condensed Matters* (Springer-Verlag Berlin Heidelberg, Berlin, 2012).
- [34] T. L. Hughes, *Topological Insulators and Topological Superconductors* (Princeton University Press, Princeton, 2013).
- [35] C. Poli, M. Bellec, U. Kuhl, F. Mortessagne, and H. Schomerus, Selective enhancement of topologically induced interface states in a dielectric resonator chain, *Nat. Commu.* **6**, 6710 (2015).
- [36] Y. G. Peng, C. Z. Qin, D. G. Zhao, Y. X. Shen, X. Y. Xu, M. Bao, H. Jia, and X. F. Zhu, Experimental demonstration of anomalous Floquet topological insulator for sound, *Nat. Commun.* **7**, 13368 (2016).
- [37] Y. G. Peng, Y. X. Shen, D. G. Zhao, and X. F. Zhu, Low-loss and broadband anomalous floquet topological insulator for airborne sound, *Appl. Phys. Lett.* **110**, 173505 (2017).
- [38] X. J. Zhang, M. Xiao, Y. Cheng, M. H. Lu, and J. Christensen, Topological sound, *Commun. Phys.* **1**, 97 (2018).
- [39] Z. G. Geng, Y. G. Peng, Y. X. Shen, D. G. Zhao, and X. F. Zhu, Topologically protected edge transport of sound in coupled cavities of a modified honeycomb lattice, *J. Phys.: Condens. Matter* **30**, 345401 (2018).
- [40] Z. G. Geng, Y. G. Peng, Y. X. Shen, D. G. Zhao, and X. F. Zhu, Acoustic delay-line filters based on largely distorted topological insulators, *Appl. Phys. Lett.* **113**, 033503 (2018).
- [41] Y. G. Peng, Y. Li, Y. X. Shen, Z. G. Geng, J. Zhu, C. W. Qiu, and X. F. Zhu, Chirality-assisted three-dimensional acoustic Floquet lattices, *Phys. Rev. Res.* **1**, 033149 (2019).
- [42] Z. G. Geng, Y. G. Peng, P. Q. Li, Y. X. Shen, D. G. Zhao, and X. F. Zhu, Mirror-symmetry induced topological valley transport along programmable boundaries in a hexagonal sonic crystal, *J. Phys.: Condens. Matter* **31**, 245403 (2019).
- [43] Z. G. Geng, Y. G. Peng, Y. X. Shen, Z. Ma, R. Yu, J. H. Gao, and X. F. Zhu, Topological nodal line states in three-dimensional ball-and-stick sonic crystals, *Phys. Rev. B* **100**, 224105 (2019).
- [44] Y. J. Ding, Y. G. Peng, Y. F. Zhu, X. D. Fan, J. Yang, B. Liang, X. F. Zhu, X. G. Wang, and J. C. Cheng, Experimental Demonstration of Acoustic Chern Insulators, *Phys. Rev. Lett.* **122**, 014302 (2019).
- [45] S. Longhi, Topological pumping of edge states via adiabatic passage, *Phys. Rev. B* **99**, 155150 (2019).
- [46] A. Messiah, *Quantum Mechanics* (North-Holland, Amsterdam, 1962).
- [47] K. Ding, G. C. Ma, M. Xiao, Z. Q. Zhang, and C. T. Chan, Emergence, Coalescence, and Topological Properties of Multiple Exceptional Points and Their Experimental Realization, *Phys. Rev. X* **6**, 021007 (2016).
- [48] K. Ding, G. C. Ma, Z. Q. Zhang, and C. T. Chan, Experimental Demonstration of an Anisotropic Exceptional Point, *Phys. Rev. Lett.* **121**, 085702 (2018).